



HAL
open science

Evaluation of the impact of freezing technique on pore-structure characteristics of highly decomposed peat using X-ray micro-computed tomography

Hassan Al Majou, Ary Bruand, Olivier Rozenbaum, Emmanuel Le Trong

► To cite this version:

Hassan Al Majou, Ary Bruand, Olivier Rozenbaum, Emmanuel Le Trong. Evaluation of the impact of freezing technique on pore-structure characteristics of highly decomposed peat using X-ray micro-computed tomography. *International Agrophysics*, 2022, 36 (3), pp.223-233. 10.31545/intagr/152057 . insu-03810010

HAL Id: insu-03810010

<https://insu.hal.science/insu-03810010>

Submitted on 11 Oct 2022

HAL is a multi-disciplinary open access archive for the deposit and dissemination of scientific research documents, whether they are published or not. The documents may come from teaching and research institutions in France or abroad, or from public or private research centers.

L'archive ouverte pluridisciplinaire **HAL**, est destinée au dépôt et à la diffusion de documents scientifiques de niveau recherche, publiés ou non, émanant des établissements d'enseignement et de recherche français ou étrangers, des laboratoires publics ou privés.



Distributed under a Creative Commons Attribution - NonCommercial - NoDerivatives 4.0 International License

Evaluation of the impact of freezing technique on pore-structure characteristics of highly decomposed peat using X-ray micro-computed tomography**

Hassan Al Majou^{1,2*}, Ary Bruand¹, Olivier Rozenbaum^{1,3}, and Emmanuel Le Trong¹

¹University of Orleans, CNRS, BRGM, Earth Sciences Institute of Orléans (ISTO), 1A rue de la Férellerie, 45071 Orleans Cedex 2, France

²University of Damas, Department of Soil Science, Faculty of Agronomy, PO Box 30621, Damas, Syria

³CNRS, Extreme conditions and Materials, High Temperature and Irridiation (CEMHTI), UPR 3079, Avenue de la Recherche Scientifique, 45071 Orleans, Cedex 2, France

Received May 25, 2022; accepted July 12, 2022

Abstract. The modelling of peatland functioning requires detailed knowledge of the peat structure. To this end, freezing is nowadays increasingly used to obtain X-ray micro computed tomography (X-ray -CT) images. The aim of this study was to analyze the structure of a peat material before freezing and post-defreezing using X-ray -CT and to look for possible alterations in the structure by analyzing the air-filled porosity. A highly decomposed peat material close to water saturation was selected for study. Three samples were analyzed before freezing and post-defreezing using an X-ray -CT Nanotom 180NF. Results showed that the continuity and cross section of the air-filled tubular pores several hundreds to about one thousand micrometers in diameter were altered post-defreezing. Many much smaller air-filled pores not detected before freezing were also recorded post-defreezing. Detailed analysis showed a dramatic increase in the number of air-filled pores ranging between 1 voxel ($216 \cdot 10^3 \mu\text{m}^3$) and 50 voxels ($10.8 \cdot 10^6 \mu\text{m}^3$) in volume. The volume of these pores newly occupied by air using X-ray -CT and their total volume was found to be consistent with the one calculated as resulting from the increase in the specific volume of water when it turns into ice.

Keywords: freezing technique, peat pore structure, image analysis, X-ray computed tomography

INTRODUCTION

In many peatland studies, the description of the physical characteristics of peat is derived from just a few basic metrics such as porosity, bulk density and humification indexes (Michel *et al.*, 2001; Quinton *et al.*, 2009; Michel, 2015; Kurnain and Hayati, 2016). However, both the short- and long-term modelling of peatland functioning, and in particular the impact of anthropogenic warming and direct human disturbance on atmospheric CO_2 , CH_4 and N_2O , requires a detailed knowledge of the peat structure and of both water and gas flow with respect to the groundwater table level (*e.g.* Gharedaghloo *et al.*, 2018; Zhao *et al.*, 2020; Glaser *et al.*, 2021; Müller and Fortunat, 2021; Swinnen *et al.*, 2021; Wiedeveld *et al.*, 2021). In order to achieve this, X-ray Computed Tomography, which is widely used in science as a non-invasive technique for the study of internal 2D and 3D structures, is a promising technique with which to analyse the structure of peats and their physical properties. Improvements in resolution have led to the development of X-ray micro-computed tomography (X-ray μ -CT), which has been applied to peat materials. Kettridge and Binley

*Corresponding author e-mail: almajou@yahoo.fr

**This work was financially supported by the Labex Voltaire (AND-10-LABX-100-01, 2009 to 2025) and the French program PAUSE (2017 to 2022).

(2008, 2011) used X-ray μ -CT to investigate gas content and peat structure. They studied samples 7.2 cm long and 7.2 cm in diameter with a resolution of 100 μm . Quinton *et al.* (2009) analysed the structure and hydraulic properties of peats using X-ray CT. They studied samples 10 cm long and 6 cm in diameter with a resolution of 45 μm and showed how water contents recorded in the field are related to the inter-particle pore-volume distribution. Using the methodology developed by Quinton *et al.* (2009), Rezanezhad *et al.* (2009, 2010) studied the influence of pore-size geometry on the hydraulic conductivity of peat by combining X-ray μ -CT and digital image processing. They found that a large reduction in unsaturated conductivity with depth was essentially controlled by the proportion of air-filled pores. More recently, Turberg *et al.* (2014) used X-ray μ -CT to analyse various degrees of disturbance related to the process of peat extraction, by working with large samples of $15 \times 15 \times 45 \text{ cm}^3$ in volume and a medical X-ray scanner. 3-D images of regular parallelepipeds of $2 \times 2 \times 14 \text{ cm}^3$ in volume were recorded with a resolution of 371 μm .

Due to the low consistency of peat materials, and the resulting possible alteration in their structure, during the process of subsampling of the peat blocks collected in the field, several authors applied freezing before extraction in order to avoid deformation during subsampling. This strategy achieves small undisturbed samples, thereby making it possible to increase the resolution of the 3D X-ray μ -CT images recorded. The peat samples collected by Kettridge and Binley (2008) were frozen soon after collection, and then defrosted prior to their study but the reason for freezing the samples remains unclear, and appears to have been motivated more by storage conditions than by considerations concerning subsampling methodology. Quinton *et al.* (2009) and Rezanezhad *et al.* (2010) froze peat blocks at -10°C for 48 h before subsampling cores 10 cm long and 6 cm in diameter which were extracted using a hollow drill bit mounted on a drill press. Gharedaghlou *et al.* (2018) used data from Rezanezhad *et al.* (2009, 2010) and modelled water and solute transport in the pore network of the $9.92 \times 9.92 \times 9.92 \text{ mm}^3$ samples, these models were extracted from X-ray μ -CT images of the peat materials. They showed that a decrease in hydraulic conductivity with depth was related to a reduction in pore radius and an increase in tortuosity. Improvements in the X-ray μ -CT technique have led to an increase in image resolution, requiring the use of smaller samples; this evolution will inevitably lead to an increasing recourse to a freezing phase in order to obtain samples with the appropriate size before analysis.

The question arises, however, as to whether freezing impacts the evolution of the soil structure. When water transitions from the liquid to the solid state, its volume increases by 8.7% (the density of ice is 0.92 g mL^{-1} while that of the liquid is 1 g mL^{-1}). While investigating the effects of freezing on the physical properties and wettability of highly decomposed peats used as growing media,

Michel (2015) showed that freezing was accompanied by a decrease in bulk density and a marked change in water retention properties but the pore structure was not analysed. Wang *et al.* (2017) used X-ray μ -CT and showed that non-uniform volumetric shrinkage, which is indicated by the freeze-necking phenomenon, was observed in an unsaturated clay soil in a closed freeze-thaw experiment. Liu *et al.* (2021) studied the impact of freeze-thaw cycles on the pore-structure characteristics of silty soil using X-ray μ -CT with a 25 μm resolution on the volume of interest, namely $8.75 \times 8.75 \times 8.75 \text{ mm}^3$. Results showed an increase in the macroporosity and pore-throat network complexity. Ma *et al.* (2021) studied the effect of freeze-thaw cycles on the pore distribution in soil aggregates 5-7 mm in diameter using 3D images with a 3.25 μm resolution, these were produced by synchrotron-based X-ray μ -CT. The results showed how the creation of pores resulting from freeze-thaw cycles may be used to explain changes in the stability of aggregates.

As the properties of porous materials are determined by macro- and micropore distribution and topology (Vogel, 2002), it is important to pay close attention to the quality of the pore distribution and topology description resulting from X-ray μ -CT analysis. The latter can only be used to study air-filled pores which are therefore the only imaged-pores thereafter according to the resolution of the X-ray μ -CT used, as those occupied by water are very difficult to distinguish from the water-saturated organic matrix. The possible alteration of both the pore network geometry and its degree of saturation during sample preparation therefore remains a concern. However, to date little attention has been paid to the possible alteration of the pore network during sample preparation which requires freezing in order to obtain subsamples with a size suitable for the desired resolution with the X-ray μ -CT used. At present, freezing is increasingly being used to obtain small size samples of peat materials for X-ray μ -CT analysis, the objective of this study was to analyse a highly decomposed peat material before freezing and post defreezing using X-ray μ -CT in order to assess whether or not freezing modified its structure by analysing the air-filled imaged-pores before and after the freeze-thaw process.

MATERIALS AND METHODS

Highly decomposed *Sphagnum* and *Molinia* peat was sampled in triplicate (samples A, B and C) from sites which were intensively studied by D'Angelo *et al.* (2016) and Bernard-Jannin *et al.* (2018) (Fig. 1). A highly decomposed peat was selected for study because it is potentially highly sensitive to the creation of structure artifacts during freezing due to its high water content and low fibre content. Large undisturbed samples ($15 \times 15 \times 25 \text{ cm}^3$) were collected from a depth of between 25 and 40 cm in order to avoid the heterogeneity of the top 20 cm due to *Molinia* roots. They

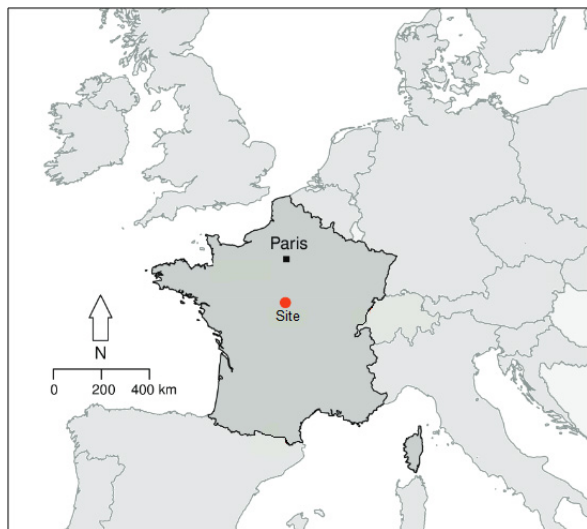


Fig. 1. Geographical location of the study site.

were collected when the groundwater table level was close to the soil surface by carefully cutting the $15 \times 15 \times 25 \text{ cm}^3$ parallelepiped volume with a large sharp knife to avoid deformation during collection. The samples were wrapped with a plastic film and placed in a rigid box to avoid deformation, this box was then sealed with a plastic bag to avoid water loss and finally stored at $3\text{--}4^\circ\text{C}$ to limit biological activity.

Bulk density and particle density were determined by using undisturbed peat samples which were a dozen cubic centimetres in volume and applying the kerosene method developed by Monnier *et al.* (1973). The total porosity was obtained by dividing the volume of water contained in a saturated sample by the known volume of the sample as described by Boelter (1976) and Nimmo (2013). The water content of the collected samples was determined after oven drying at 105°C for 24 h. The degree of peat decomposition was characterized by using the pyrophosphate index (Kaila, 1956) which was determined following Gobat *et al.* (1986). The C and N contents were determined through the combustion of dried and crushed samples at 1100°C , using a CNS-2000 LECO apparatus.

In order to obtain samples of the appropriate size for X-ray $\mu\text{-CT}$, subsamples of peat material with a volume of $4 \times 4 \times 7 \text{ cm}^3$ corresponding to the depth of 30–37 cm were prepared by using with a scalpel blade to limit the disturbance of the peat structure as far as possible. Then each sample was placed in a transparent PVC tube 5 cm in diameter which was then hermetically sealed with a screw cap to avoid water loss. The samples were first imaged using X-ray $\mu\text{-CT}$ and then, on the basis of the methodology developed and used by Rezanezhad *et al.* (2010), Ramirez *et al.* (2016) and Moore *et al.* (2017), they were frozen at -10°C for 48 h, defrosted for 48 h at 20°C and imaged again X-ray $\mu\text{-CT}$. Each sealed PVC tube was weighed with its

peat material at different steps of the process, *i.e.*, prior to and after each X-Ray $\mu\text{-CT}$ imaging process, to check for the absence of water loss during the acquisition of the projected 2D images. Measurements showed that the weight variation between two successive steps and between the first and last step was $<0.03 \text{ g}$ for the two samples studied. This amount loss was considered to be negligible.

X-ray $\mu\text{-CT}$ was performed for the subsamples $4 \times 4 \times 7 \text{ cm}^3$ in volume using the Nanotom 180NF micro X-ray $\mu\text{-CT}$ device (GE Phoenix|x-ray, Wunstorf, Germany). This equipment has a 180-kV nanofocus X-ray tube and a digital detector array (2304×1152 pixels, Hamamatsu detector). The samples were placed in the chamber and rotated by 360 degrees during acquisition. The samples were centred and waxed on a sample holder (circular plate) the axis of rotation of which was collinear to that of the tomograph chuck. An operating voltage of 120 kV and a filament current of $100 \mu\text{A}$ were applied. The distance between the X-ray source and the sample and between the X-ray source and the detector was 300 and 500 mm, respectively, giving a voxel size of $60 \mu\text{m}$. The tomograph detector recorded 2D projections in 16 bit, *i.e.* divided into 65536 grey levels. The resulting projections were converted into a 3D image stack using a microcluster of four personal computers (PCs) with Phoenix 3D reconstruction software. A filtered backprojection algorithm was used according to the method of Feldkamp *et al.* (1984). The reconstruction software contained several different modules for artifact reduction (beam hardening, ring artifacts) in order to optimize the results. After reconstruction, the images were recorded in 8 bit (256 levels of grey) by always checking that the histograms of the 16-bit and 8-bit images were similar and that the images were visually indistinguishable. During this process, we increased the dynamic range of the image by spreading the histogram over the entire range between 0 and 255 levels of grey. This facilitated the subsequent segmentation step. The 2000 projection images (with an angular increment of 0.18°) were acquired during sample rotation (with an acquisition time of 4 h) for every sample before freezing and post defreezing. As the cone beam geometry created artifacts, the first and the last 76 cross-sectional images were removed (Le Trong *et al.*, 2008; Rozenbaum and Rolland du Roscoat, 2014).

The resulting 3D images were cropped for sample A to a size of $430 \times 600 \times 800$ voxels corresponding to $2.6 \times 3.6 \times 4.8 \text{ cm}^3$ before freezing and post defreezing, and for samples B and C to a size of $430 \times 530 \times 850$ voxels before freezing and post defreezing corresponding to $2.6 \times 3.2 \times 5.1 \text{ cm}^3$, with a voxel size of $60 \times 60 \times 60 \mu\text{m}^3$.

X-ray image analysis was performed using a custom developed code written in C++. A region of interest that excluded the irregular sample boundaries and outside region was defined for every sample by identifying the largest rectangular parallelepiped image in the cylindrical sample studied. Smoothing the 3D images with a moving average

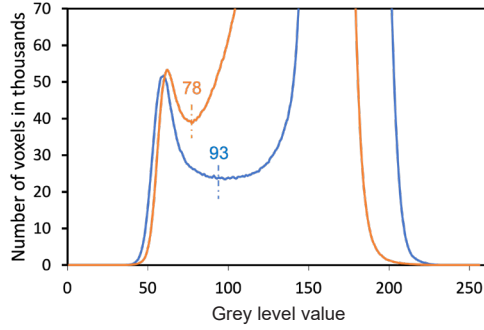


Fig. 2. Distribution of the grey level values in the 3D X-ray μ -CT images which were recorded before freezing (blue) and post freezing (red) for sample A. The grey level values corresponding to the threshold value between the air-filled pores and the water-saturated porous organic matrix are also plotted.

filter over a window of $5 \times 5 \times 5$ voxels increased their signal-to-noise ratios from the range of 7.6-9.2 to 12.5-15.0. The moving average filter replaced each voxel of the original image by the average grey value of its neighbours over a window centred on it as this is considered to be the optimal method to remove random noise on grey-level images (Smith, 1997). The signal-to-noise ratio was assumed to be the ratio of the average of the grey levels of the image to their standard deviation according to Avcibas *et al.* (2002). They were then classified using thresholding. The threshold value used was the absolute minimum value between the two peaks of the bimodal distribution of the grey levels of the voxels of each image (Fig. 2) (Rozenbaum *et al.*, 2012). The grey level corresponding to the threshold value for sample A before freezing and post defreezing was 93 and 78, respectively, and for samples B and C before freezing and post defreezing, it was 80 and 68, respectively. The voxels with a grey level lower than the threshold value were considered to be pore voxels while those with a grey level higher than or equal to the threshold value were considered to be matrix voxels. This simple procedure has no adjustable parameter and therefore introduces no bias when comparing the images. For each binary image, each pore (*i.e.*, group of contiguous foreground voxels surrounded by matrix voxels) was identified by a voxel-by-voxel scan of the image, and its volume (in terms of number of voxels) was recorded by applying the following algorithmic procedure:

- Consider each voxel during a raster scan of the image. Let v be the current voxel.
- If v is a matrix voxel, or has been classified as belonging to an already identified pore, proceed to the next voxel.
- If v is a pore voxel belonging to an as yet unidentified pore, starting from v , perform a geodesic reconstruction of the pore (Lantuéjoul and Beucher, 1981). During the reconstruction of the pore, classify all of its voxels as belonging to an identified pore, and keep track of their

number. Once the reconstruction is complete, the number of voxels yields the volume of the pore. Proceed to the next voxel in the raster scan.

The outcome of this procedure is a list of the pores, their volume and their position in the 3D image. The total porosity is then the ratio of the total pore volume divided by the total volume of the rectangular parallelepiped selected.

The total porosity before freezing ($\phi_{T,BF}$) may be written as follows:

$$\phi_{T,BF} = \frac{V_{V,BF}}{V_S + V_{V,BF}}, \quad (1)$$

where: $V_{V,BF}$ is the total specific volume of the pores of the peat material before freezing ($\text{cm}^3 \text{g}^{-1}$), V_S is the specific volume of the organic solid phase dried at 105°C ($\text{cm}^3 \text{g}^{-1}$) (reciprocal of the particle density). Then, using Eq. (1):

$$V_{V,BF} = \frac{\phi_{T,BF} V_S}{1 - \phi_{T,BF}}. \quad (2)$$

The specific volume of the pores before freezing, $V_{V,BF}$, may be expressed as follows:

$$V_{V,BF} = V_{V,Mwf,BF} + V_{V,TPwf,BBF} + V_{V,TPaf,BF}, \quad (3)$$

where: $V_{V,Mwf,BF}$ is the specific volume of the pores of the organic matrix saturated with water before freezing ($\text{cm}^3 \text{g}^{-1}$), $V_{V,TPwf,BBF}$ is the specific volume of the tubular pores occupied with water before freezing ($\text{cm}^3 \text{g}^{-1}$) and $V_{V,TPaf,BF}$ is the specific volume of tubular air-filled pores before freezing ($\text{cm}^3 \text{g}^{-1}$). The porosity related to the tubular air-filled pores before freezing, $\phi_{TPaf,BF}$, may be expressed as follows in the whole peat material:

$$\phi_{TPaf,BF} = \frac{V_{V,TPaf,BF}}{V_S + V_{V,BF}}. \quad (4)$$

Thus:

$$V_{V,TPaf,BF} = \phi_{TPaf,BF} (V_S + V_{V,BF}), \quad (5)$$

with the values of $\phi_{TPaf,BF}$ corresponding to the value of ϕ measured before freezing using X-ray μ -CT.

The increase in the specific volume of liquid water by 8.7% when it freezes as the temperature transitions from 20°C to -10°C (Harvey, 2017) increases the porosity of both the pores in the organic matrix and the tubular pores filled with water before freezing resulting in a porosity post defreezing which may be calculated as follows:

$$\phi_{Mwf,AF} + \phi_{TPwf,AF} = \frac{(V_{V,Mwf,BF} + V_{V,TPwf,BF})1.087}{V_S + ((V_{V,Mwf,BF} + V_{V,TPwf,BF})1.087) + V_{V,TPaf,BF}}, \quad (6)$$

where: $\varphi_{Mwf, AF}$ is the porosity related to the water-filled organic matrix post defreezing, $\varphi_{TPwf, AF}$ is the porosity related to the water-filled tubular pores post defreezing, and 1.087 is the coefficient by which the volume of water is increased when it transitions from liquid (20°C) to solid (-10°C). Using Eq. (3):

$$\varphi_{Mwf, AF} + \varphi_{TPwf, AF} = \frac{(V_{V, BF} - V_{V, TPwf, BF})1.087}{V_S + ((V_{V, BF} - V_{V, TPwf, BF})1.087) + V_{V, TPwf, BF}} \quad (7)$$

These values may be compared to those of $\varphi_{Mwf, BF} + \varphi_{TPwf, BF}$ before freezing which may be calculated as follows:

$$\varphi_{Mwf, BF} + \varphi_{TPwf, BF} = \varphi_T - \varphi_{TPwf, BF}, \quad (8)$$

with $\varphi_{TPwf, BF}$ being equal to φ before freezing.

RESULTS AND DISCUSSION

The measured physical characteristics of the peat samples studied are given in Table 1. The volumetric water contents at the time of sampling were similar for the three samples A, B and C (0.893, 0.883 and 0.890 cm³ cm⁻³, respectively). These values are much higher than those recorded by Rezanezhad *et al.* (2010) for sphagnum peat materials (between 0.38 and 0.43 cm³ cm⁻³) which were collected between the surface and a 67 cm depth. Their peat materials were collected far from the point of water saturation because the groundwater table level was far below the surface, whereas our samples were collected while the groundwater table level was close to the soil surface. The porosity values of samples A, B and C (0.918, 0.904 and 0.911, respectively) are close to their water content, thus indicating that they were close to the point of water saturation (97.1, 98.1 and 97.1 %, respectively). The measured bulk densities recorded for the three samples A, B and C (0.135, 0.178 and 0.142 g cm⁻³, respectively) are consistent with those of highly decomposed peat materials (Benscoter *et al.*, 2011; Kurnain and Hayati, 2016). The measured pyrophosphate indices recorded for samples A, B and C (96.1, 78.9 and 81.2, respectively) are also consistent with highly decomposed peat materials which may be classified as asapric peat (pyrophosphate index >30) according to Levesque *et al.* (1980). The C/N ratio recorded for samples

A, B and C (12.1, 16.6 and 15.0, respectively) confirms that the three peat samples present a high degree of decomposition (Comont *et al.*, 2006). Finally, the dry bulk density values recorded for the three samples A, B and C (0.135, 0.178 and 0.142 g cm⁻³, respectively) are much closer to the values recorded for a well-decomposed peat material resulting from *Sphagnum* moss with a fibre content of only 15% (0.250 g cm⁻³) than to the values recorded for undecomposed peat materials with a fibre content of 98% (0.009 g cm⁻³) (Boelter, 1968). Overall, the peat material selected for this study is in a much more advanced state of decomposition than the peat materials studied by Quinton *et al.* (2009) and Rezanezhad *et al.* (2010).

The same heights were chosen for the 3D X-ray μ -CT images in grey levels before freezing and post defreezing for samples A (800 voxels), B and C (850 voxels). The final image sizes chosen were then 430×600×800 voxels (~2.6×3.6×4.8 cm³) before freezing and post defreezing for sample A and 430×530×850 voxels (~2.6×3.2×5.1 cm³) before freezing and post defreezing for samples B and C.

The grey level of the images was determined by the absorption of the incident X-ray radiation by the different phases of the peat material. The absorption of each phase depends on its density and the mean atomic number resulting from its chemical composition (Youn *et al.*, 2015). It may be described by the Beer-Lambert law:

$$I = I_o \exp(-\mu x), \quad (9)$$

where: I is the transmitted X light, I_o is the incident X light, μ is the absorption coefficient, and x is the path length. As a consequence, the intensity of the transmitted X light which results in a grey level of the pixel in the 2D images and of the voxel in the 3D images depends on the proportion of air, water and organic compounds in the pixel or voxel considered. Because of the weak difference between the mean atomic number assumed for the porous organic matrix of a highly decomposed and water-saturated peat material (Table 1) and the mean atomic number of the water phase, we may assume that the absorption coefficient of these two phases is very close. Therefore, only the air phase may be distinguished from the other phases. Thus, only the air-filled pores are identifiable on the 2D and 3D images; the pores occupied by water are indistinguishable from the water-saturated porous organic matrix.

Table 1. Main physical and chemical characteristics of samples A, B and C of the highly decomposed peat material studied

Sample	Depth (cm)	$\varphi_{T, BF}$	D_p	θ (cm ³ cm ⁻³)	D_b (g cm ⁻³)	PPI	C:N
A	25-40	0.918	1.692	0.893	0.135	96.1	12.1
B	25-40	0.904	1.779	0.883	0.178	78.9	16.6
C	25-40	0.911	1.714	0.890	0.142	81.2	15.0

$\varphi_{T, BF}$ – total porosity before freezing, D_p – particle density, θ – water content at sampling, D_b – bulk density, PPI – pyrophosphate index.

Pairs of 2D X-ray μ -CT images recorded before freezing and post defreezing were selected from within the pairs of stacks of 2D images by identifying the closest images in terms of the morphology of air-filled pores of a few hundred micrometres in size. These imaged-pores are shown in very dark grey in Fig. 3. The lighter dark grey background corresponds to the highly decomposed organic material and the related imaged-porosity which was filled by water. For each pair of 2D X-ray μ -CT images, a comparison showed the presence of (i) imaged-pores which are recognizable on the images before freezing and which were still present post defreezing but exhibiting a different morphology, (ii) imaged-pores are recognizable on the images before freezing which were not present post defreezing, (iii) and the presence of imaged-pores which are recognizable post defreezing and which were not present before freezing (Fig. 3). Observation of the 2D X-ray μ -CT images also showed no apparent damage to the peat material which may have resulted from the subsampling procedure and then the introduction of the subsample into the PVC tube for X-ray μ -CT measurements. However, the use of pairs of 2D X-ray μ -CT images does not allow for an accurate estimation of the possible evolution of the imaged-porosity of peat materials during the freezing process since it was not possible to be reasonably confident that the pairs of 2D images corresponded exactly to the same slice in the sample before and post defreezing. Only a 3D analysis is able to establish whether the imaged-porosity of the peat materials is different before and post defreezing.

The 3D X-ray μ -CT binary images of the two samples A and B were first morphologically compared globally by comparing the imaged-porosity which was characterized by X-ray μ -CT before freezing and post defreezing (Fig. 4a and d). The results showed that the air-filled pore measurements corresponded to a very small proportion

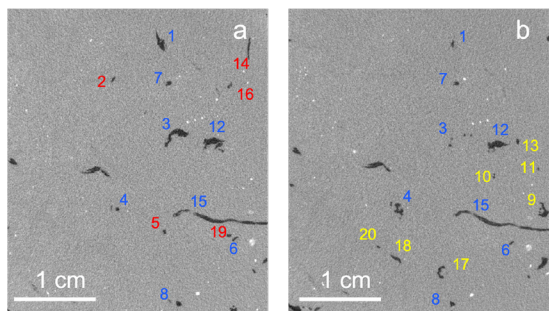


Fig. 3. Pairs of 2D μ -CT images taken of sample A before (a) and post defreezing (b) were extracted from the 3D X-ray μ -CT images in grey levels showing air-filled pores (very dark grey), and the solid organic material with water filling the associated pores (dark grey) and particles of iron oxy-hydroxides (very light grey). The numbers identify the pores which were present before freezing (a) and they were still present post defreezing (b) but with a different shape or size (blue), those present before freezing and not post defreezing (red) and not present before freezing but present post defreezing (yellow).

of the total porosity of the peat material studied, less than 0.02, whereas the total porosity of samples A, B and C were determined by using the water content when the samples were saturated, these values were 0.918, 0.904 and 0.911 before freezing, respectively (Tables 1 and 2). Indeed, most of the porosity present in the samples corresponded to both very small water-filled pores which are closely associated to the solid phase which corresponds to highly decomposed organic compounds and potentially also to larger water-filled pores that were indistinguishable from the porous water saturated organic matrix.

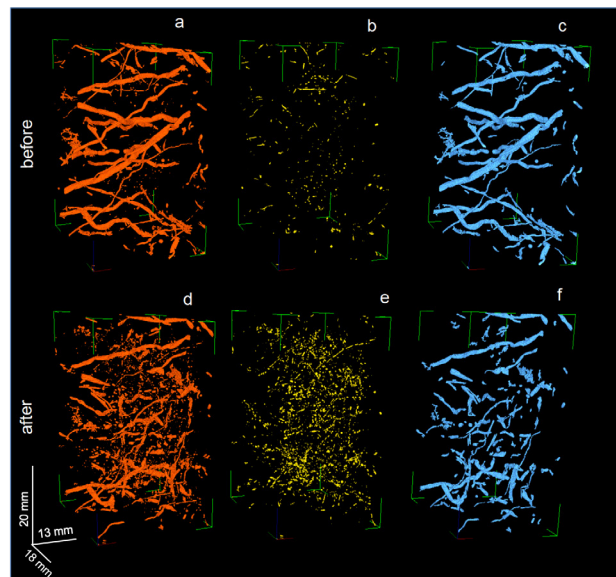


Fig. 4. 3D X-ray μ -CT binary images of $430 \times 600 \times 800$ voxels in volume ($\sim 2.6 \times 3.6 \times 4.8$ cm³) from sample A showing pores detected before freezing (a) and post defreezing (d), the pores smaller than 500 voxels in volume before freezing (b) and post defreezing (e), and the pores larger than 500 voxels in volume before freezing (c) and post defreezing (f).

Table 2. Characteristics of the pores in the 3D X-ray CT images of samples A, B and C of the highly decomposed peat material studied before freezing and post defreezing

Sample	ϕ	Number of pores	Average size of the pores (voxels)
Sample A			
Before freezing	0.009	470	3952
Post-defreezing	0.017	4792	732
Sample B			
Before freezing	0.005	474	2043
Post-defreezing	0.011	4371	488
Sample C			
Before freezing	0.007	475	2998
Post-defreezing	0.015	4607	610

ϕ – imaged-porosity measured in 3D X-ray CT.

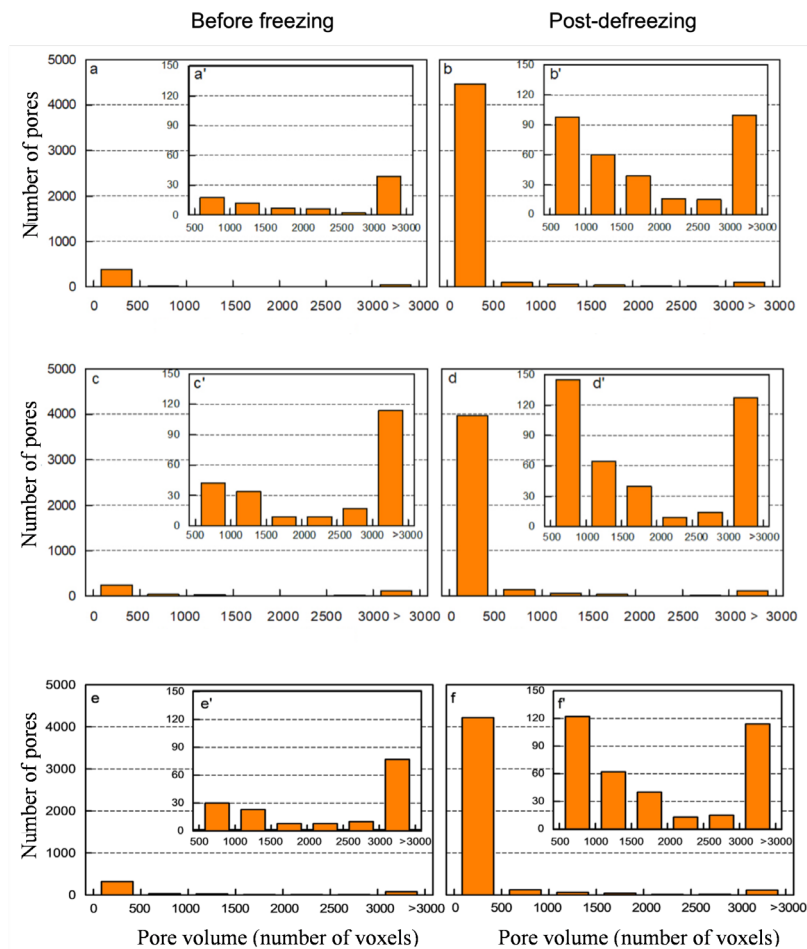


Fig. 5. Pore-volume distribution according to the number of voxels of $60 \times 60 \times 60 \mu\text{m}^3$ in volume in the 3D X-ray μ -CT images of sample A before freezing (a, a') and post defreezing (b, b'), sample B before freezing (c, c') and post defreezing (d, d'), and sample C before freezing (e, e') and post defreezing (f, f').

The number of air-filled pores was however very different before freezing and post defreezing for the three samples studied. There were 470, 474 and 475 air-filled pores before freezing, and 4792, 4371 and 4607 air-filled pores post defreezing for samples A, B and C, respectively (Table 2). Whatever the origin of the new air-filled pores, the results showed a strong decrease in the average size of the air-filled pores post defreezing, from 3952 to 732 voxels, from 2043 to 488 voxels and from 2998 to 610 for samples A, B and C, respectively (Table 2).

An analysis of the pore-size distribution showed that the increase in the number of air-filled pores was mainly related to an increase in the number of pores of <500 voxels in volume (*i.e.*, $<0.108 \text{ mm}^3$) (Fig. 5a, b, c, d, e, and f). The air-filled pores of >500 voxels were also highly affected (Fig. 5a', b', c', d', e' and f'). After the separation of the air-filled pores that were larger and smaller than 500 voxels in volume, the 3D X-ray μ -CT images showed that the morphology of the air-filled pores of >500 voxels was affected, with alterations in both their continuity and transversal section size (Fig. 4c and f). An analysis of the

distribution of the pores of <500 voxels in volume showed a strong increase in the number of pores of all sizes, with the highest increase being recorded for pores ranging from 1 to 50 voxels in volume (Fig. 6). The results also showed that the number of air-filled pores in every class of pore volume was significantly different before and post defreezing (Table 3).

Subimages of the 3D X-ray μ -CT images recorded were selected in order to compare the differences in pore morphology qualitatively before freezing and post defreezing more easily than is the case with the whole images in which the high number of pores limited the morphological analysis (Fig. 4), particularly for the pores of <500 voxels (Fig. 4b and e). Thus, one 3D X-ray μ -CT subimage of $200 \times 350 \times 350$ voxels in volume ($\sim 1.2 \times 2.12.1 \text{ cm}^3$) was selected for sample A (Fig. 7). The selected subimages showed that pores of <500 voxels corresponded to air-filled pores of several voxels to several dozen voxels, and also to discontinuous air-filled fine tubular pores (Fig. 7b and e). The comparison showed that freezing led to a dramatic

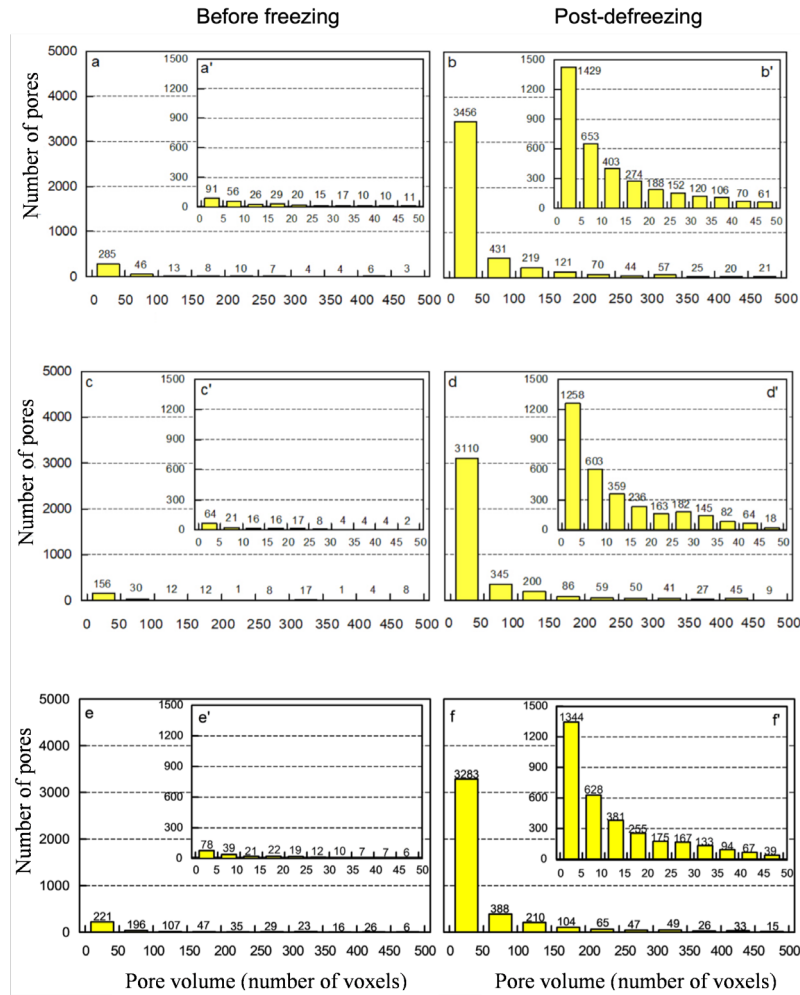


Fig. 6. Pore-volume distribution according to the number of voxels (≤ 500) and (≤ 50), of $60 \times 60 \times 60 \mu\text{m}^3$ in volume in the 3D X-ray μ -CT images of sample A before freezing (a, a'), and post defreezing (b, b'), and of sample B before freezing (c, c'), and post defreezing (d, d').

Table 3. Descriptive statistics of the air-filled pores detected before freezing and post defreezing of the three samples A, B and C studied

	Pore volume (number of voxels)						
	≤ 500	500-1000	1000-1500	1500-2000	2000-2500	2500-3000	>3000
Number of pores before freezing							
Mean	307**	25**	19***	7*	7*	7*	64**
S.d.	71	14	13	2	2	8	44
Min.	249	16	12	5	5	2	39
Max.	386	42	34	9	9	17	114
Number of pores post-defreezing							
Mean	3413**	97**	50***	32*	10*	12*	91**
S.d.	1415	49	21	13	5	5	42
Min.	1804	47	25	17	6	6	45
Max.	4464	145	64	40	16	15	127

S.d. – Standard deviation, means for every class of air-filled pores were significantly different: *** $p \leq 0.001$, ** $p \leq 0.01$ and * $p \leq 0.05$.

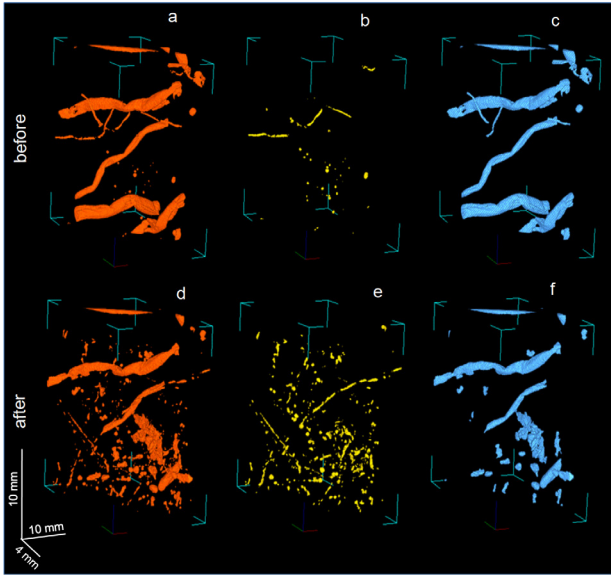


Fig. 7. 3D X-ray μ -CT binary subimages of $200 \times 350 \times 350$ voxels in volume ($\sim 1.2 \times 2.1 \times 2.1 \text{ cm}^3$) of sample A showing all the pores detected before freezing (a) and post defreezing (d), the pores smaller than 500 voxels in volume before freezing (b) and post freezing (e), and the pores larger than 500 voxels in volume before freezing (c) and post freezing (f).

increase in the number of air-filled pores (Fig. 6) and to the appearance or disappearance of discontinuous air-filled fine tubular pores of < 500 voxels (Fig. 7b and e).

As freezing leads to an 8.7% increase in the specific volume of the water (Harvey, 2017), the possible consequences of this increase on the changes recorded for the peat material studied were analysed. Thus, V_S was found to be equal to 0.591, 0.562, and 0.583 $\text{cm}^3 \text{g}^{-1}$ for samples A, B and C, respectively (the reciprocal of the particle density measured for peat materials A, B and C) (Table 1), and Eq. (2) gives $V_{V, BF}$ values of 6.616, 5.292, and 5.968 $\text{cm}^3 \text{g}^{-1}$ for samples A, B and C, respectively. The specific volume of the pores before freezing, $V_{V, BF}$, being composed according to Eq. (3) of $V_{V, Mwf, BF}$, $V_{V, TPwf, BF}$ and $V_{V, TPaf, BF}$, the latter was computed by using Eq. (5) which gives $V_{V, TPaf, BF} = 0.065, 0.029, \text{ and } 0.046 \text{ cm}^3 \text{g}^{-1}$ for samples A, B and C, respectively, with the values of $\phi_{TPaf, BF}$ required by Eq. (5) corresponding to the value of ϕ which was measured before freezing by using X-ray μ -CT (Table 2).

Equation (7) enabled the calculation of $\phi_{Mwf, AF} + \phi_{TPwf, AF}$ and gives $\phi_{Mwf, AF} + \phi_{TPwf, AF}$ values of 0.916, 0.906 and 0.911 for samples A, B and C, respectively by using values of $V_{V, BF}$ and $V_{V, TPaf, BF}$ given by Eqs (2) and (5), respectively. These values can be compared to those of $\phi_{Mwf, BF} + \phi_{TPwf, BF}$ before freezing which were calculated according to Eq. (8) which gives $\phi_{Mwf, BF} + \phi_{TPwf, BF} = 0.909, 0.899 \text{ and } 0.904$ for samples A, B and C, respectively.

Thus, according to these results and their related assumptions, the increase in the water-filled porosity of samples A, B and C post defreezing was 0.007. These

values can be compared with the increase in the air-filled porosity and measured by using the 3D X-ray μ -CT images recorded in this study. This increase post defreezing was 0.008, 0.006 and 0.008 for samples A, B and C, respectively and thus similar to the calculated values.

Based on these different results, two scenarios may be proposed to explain what happened during the freeze-thaw process. According to the first scenario, during freezing, the water-filled pore volume corresponding to the sum of the pores of the organic matrix and of the fine tubular pores increases by 8.7% because of the increase in the specific volume of water when it turns from liquid to solid. After thawing to room temperature, the peat material retains the memory of this evolution during the freezing phase. As the specific pore volume of the highly decomposed organic matrix increases in volume following the formation of ice, it does not then decrease after thawing, with the result that the water, which was located preferentially in the smallest pores, small tubular pores and in the largest pores of the organic matrix, which were all saturated with water before freezing, is no longer located in these pores when the water turns from solid to liquid after thawing. The porosity which is newly occupied by air was determined by using 3D X-ray μ -CT (Table 2) and this value corresponds to the increase in porosity calculated following the transformation of liquid water into ice. The second scenario assumes that most of the small elongated pores would already be partially air-filled but at the same time their volumes are too small to be detected with the 3D X-ray μ -CT used in this study. After the completion of the freeze-thaw process, for the same reasons as for the first scenario concerning the evolution of the porous organic matrix, the proportion and size of the small air-filled pores increases, making them detectable using 3D X-ray μ -CT.

Finally, the increase in the specific volume of water due to freezing may also be responsible for the alteration of the already air-filled tubular pores of > 500 voxels as compared to their state before freezing as shown by the 3D binary images (Fig. 3) and the pore-volume distribution (Figs 5 and 6) because of deformations in the structure of the surrounding porous organic matrix during freezing.

CONCLUSIONS

1. The freezing technique which can be used prior to peat material subsampling as required by 3D X-ray μ -CT alters the structure of the highly decomposed and close to water saturation peat material studied. Both the continuity and the cross section of the air-filled tubular pores measuring from several hundred to about one thousand micrometres in diameter differed before freezing and post defreezing. These pores were several hundred to several thousand voxels in volume in the 40 cm^3 highly decomposed peat material studied, with one voxel corresponding to $216 \mu\text{m}^3$ in volume.

2. Very small air-filled pores of several voxels to several dozen voxels in volume and discontinuous air-filled fine tubular pores within the peat material studied were only detected post defreezing in the samples. The increase in the specific volume of water by 8.7% when it turns from liquid to solid because of freezing led to the creation of a pore volume in the organic matrix which remained saturated by water when it returned to room temperature. This induced the desaturation of some of the finest tubular pores as well as some of the largest pores of the porous organic matrix which were both water-filled before freezing. The volume of these pores that were newly occupied by air post defreezing was measured by using X-ray μ -CT and their cumulated volume was found to be consistent with the one calculated by taking into account the thermal expansion of water as the temperature transitioned from 20°C (liquid) to -10°C (ice).

3. The increase in the specific volume of water due to freezing is also responsible for the alteration of the already air-filled tubular pores of >500 voxels as compared to their state before freezing, as shown by the 3D binary images and the pore-volume distribution, and this alteration is a consequence of the deformation of the organic matrix due to the increase in the specific volume of water when it turns from liquid to solid due to freezing.

4. Both the pore morphology and pore-size distribution, and more globally, the structure of the highly decomposed peat material studied, were altered by freezing. Thus, the possible consequences of freezing prior to any study of the structure of peat materials should be investigated, particularly for highly decomposed peat materials. Future work will focus on the possible presence of pore geometry artifacts similar to those recorded in our study but in less decomposed peat materials, which may be less sensitive to the occurrence of artefacts post defreezing.

Conflict of interest: The authors do not declare any conflict of interest.

ACKNOWLEDGEMENT

The authors acknowledge all of the contributions which enabled us to carry out this study.

REFERENCES

- Avcibas I., Sankur B., and Sayood K., 2002.** Statistical evaluation of image quality measures. *J. Electron. Imag.*, 11(2), <https://doi.org/10.1117/1.1455011>.
- Benscoter B.W., Thompson D.K., Waddington J.M., Flannigan M.D., Wotton B.M., de Groot W.J., and Turetsky M.R., 201.** Interactive effects of vegetation, soil moisture and bulk density on depth of burning of thick organic soils. *Int. J. Wildland Fire.*, 20, 418-429, <https://doi.org/10.1071/WF08183>.
- Bernard-Jannin L., Binet S., Gogo S., Leroy F., Défarge C., Jozja N., Zocatelli R., Perdereau L., and Laggoun-Défarge F., 2018.** Hydrological control of dissolved organic carbon dynamics in a rehabilitated Sphagnum dominated peatland: a water-table based modelling approach. *Hydrol. Earth Syst. Sc.*, 22, 4907-4920, <https://doi.org/10.5194/hess-2017-578>.
- Boelter D.H., 1968.** Important physical properties of peat materials. Proc. 3rd Int. Peat Congress, August 18-23, Quebec, Canada.
- Boelter D.H., 1976.** Methods for analysing the hydrological characteristics of organic soils in marsh-ridden areas. In: *Hydrology of Marsh-Ridden Areas. Proc. IASH Symp. Minsk, 1972, IASH, UNESCO, Paris.*
- Comont L., Laggoun-Défarge F., and Disnar J.R., 2006.** Evolution of organic matter indicators in response to major environmental changes: the case of a formerly cut-over peat bog (Le Russey, Jura Mountains, France). *Org. Geochem.*, 37, 1736-1751. <https://doi.org/10.1016/j.orggeochem.2006.08.005>.
- D'Angelo B., Gogo S., Laggoun-Défarge F., Le Moing F., Jégou F., and Guimbaud C., 2016.** Soil temperature synchronisation improves representation of diel variability of ecosystem respiration in *Sphagnum* peatlands. *Agr. Forest Meteorol.*, 223, 95-102. <https://doi.org/10.1016/j.agrformet.2016.03.021>
- Feldkamp L.A., Davis L.C., and Kress J.W., 1984.** Practical cone-beam algorithm. *J. Opt. Soc. Am. A*, 1(6), <https://doi.org/10.1364/JOSAA.1.000612>.
- Gharedaghloo B., Price J.S., Rezanezhad F., and Quinton W.L., 2018.** Evaluating the hydraulic and transport properties of peat soil using pore network modeling and X-ray micro computed tomography. *J. Hydrol.*, 561, 494-508, <https://doi.org/10.1016/j.jhydrol.2018.04.007>.
- Glaser P.H., Rhoades J., and Reeve A.S., 2021.** The hydraulic conductivity of peat with respect to scaling, botanical composition, and greenhouse gas transport: mini-aquifer tests from the Red Lake Peatland, Minnesota. *J. Hydrol.*, 596, 125686, <https://doi.org/10.1016/j.jhydrol.2020.125686>.
- Gobat J.M., Grosvernier P., and Matthey Y., 1986.** Les tourbières du Jura suisse. Milieux naturels, modifications humaines, caractères des tourbes, potentiel de régénération, Actes de la Société Jurassienne d'Emulation, 213-315.
- Harvey A.H., 2017.** Properties of ice and supercooled water. In: *CRC Handbook of Chemistry and Physics (Eds W.M. Haynes, D.R. Lide, T.J. Bruno)*, Boca Raton, FL, CRC Press.
- Kaila A., 1956.** Determination of the degree of humification in peat samples. *Agric. Sci. Finl.*, 28, 18-35. <https://doi.org/10.23986/afsci.71402>
- Kaila A., 2008.** Determination of the degree of humification of peat samples. *J. Agr. Sci. Finland*, 28, 18-35, 1956.
- Kettridge N., and Binley A., 2008.** X-ray computed tomography of peat soils: measuring gas content and peat structure. *Hydrol. Process.*, 22, 4827-4837, <https://doi.org/10.1002/hyp.7097>.
- Kettridge N., and Binley A., 2011.** Characterization of peat structure using X-ray computed tomography and its control on the ebullition of biogenic gas bubbles. *J. Geophys. Res.*, 116, G01024, <https://doi.org/10.1029/2010JG001478>.

- Kurnain A., and Hayati A., 2016.** Characteristics of water retention of ombrotrophic peats under different land uses. Full Paper Proc. ETAR, Int. Conf. Emerging Trends in Academic Research, 3, 271-280, <http://eprints.ulm.ac.id/id/eprint/3165>.
- Lantuéjoul C., and Beucher S., 1981.** On the use of the geodesic metric in image analysis. *J. Microsc.*, 121, 39-49,
- Le Trong E., Rozenbaum O., Rouet J.L., and Bruand A., 2008.** A simple methodology to segment X-ray tomographic images of a multiphase building stone. *Image Anal. Stereol.*, 27, 175-182, <https://doi.org/10.5566/ias.v27.p175-182>.
- Levesque M., Diné H., and Marcoux R., 1980.** Évaluation des critères de différenciation pour la classification de 92 matériaux tourbeux du Québec et de l'Ontario, *Can. J. Soil Sci.*, 60, 479-486. <https://doi.org/10.4141/cjss80-053>.
- Liu B., Ma R.M., and Fan H.M., 2021.** Evaluation of the impact of freeze-thaw cycles on pore structure characteristics of black soil using X-ray computed tomography. *Soil Till. Res.*, 206, 104810, <https://doi.org/10.1016/j.still.2020.104810>.
- Ma R.M., Jiang Y., Liu B., and Fan H.M., 2021.** Effects of pore structure characterized by synchrotron-based micro-computed tomography on aggregate stability of black soil under freeze-thaw cycles. *Soil Till. Res.*, 207, 104855, <https://doi.org/10.1016/j.still.2020.104855>.
- Michel J.C., Rivière L.M., and Bellon-Fontaine M.N., 2001.** Measurement of the wettability of organic materials in relation to water content by capillary rise method. *Eur. J. Soil Sci.*, 52, 459-467, <https://doi.org/10.1046/j.1365-2389.2001.00392.x>.
- Michel J.C., 2015.** Effect of freezing on the physical properties and wettability of highly decomposed peats used as growing media. *Eur. J. Hort. Sci.*, 80, 190-195, doi: 10.17660/eJHS.2015/80.4.7.
- Monnier G., Stengel P., and Fiès J.C., 1973.** Une méthode de mesure de la densité apparente de petits agglomérats terreux. Application à l'analyse des systèmes de porosité du sol. *Ann. Agron.*, 25, 533-545.
- Moore P.A., Lukenbach M.C., Kettridge N., Petrone R.M., Devito K.J., and Waddington J.M., 2017.** Peatland water repellency: Importance of soil water content, moss species, and burn severity. *J. Hydrol.*, 554, 656-665, <https://doi.org/10.1016/j.jhydrol.2017.09.036>.
- Müller J., and Fortunat J., 2021.** Committed and projected future changes in global peatlands – continued transient model simulations since the Last Glacial Maximum. *Biogeosciences*, 3657-3687, <https://doi.org/10.5194/bg-18-3657-2021>.
- Nimmo J.R., 2013.** Porosity and pore size distribution. *Enc. Soil Environ.*, 3, 295-303, <https://doi.org/10.1016/B978-0-12-409548-9.05265-9>.
- Quinton W.L., Elliot T., Price J.S., Rezaezhad F., and Heck R., 2009.** Measuring physical and hydraulic properties of peat from X-ray tomography. *Geoderma*, 153, 269-277, <https://doi.org/10.1016/j.geoderma.2009.08.010>.
- Ramirez J.A., Baird A.J., and Coulthard T.J., 2016.** The effect of pore structure on ebullition from peat. *J. Geophys. Res.-Biogeo.*, 121, 1646-1656. <https://doi.org/10.1002/2015JG003289>.
- Rezaezhad F., Quinton W.L., Price J.S., Elrick D., Elliot T.R., and Heck R.J., 2009.** Examining the effect of pore size distribution and shape on flow through unsaturated peat using 3-D computed tomography. *Hydrol. Earth Syst. Sci.*, 13, 1993-2002, <https://doi.org/10.594/hessd-6-3835-2009>.
- Rezaezhad F., Quinton W.L., Price J.S., Elliot T.R., Elrick D., and Shook K.R., 2010.** Influence of pore size and geometry on peat unsaturated hydraulic conductivity computed from 3D computed tomography image analysis. *Hydrol. Process.*, 24, 2983-2994, <https://doi.org/10.5194/hess-13-1993-2009>.
- Rozenbaum O., Bruand A., and Le Trong E., 2012.** Soil porosity resulting from the assemblage of silt grains with a clay phase: New perspectives related to utilization of X-ray synchrotron computed microtomography. *C.R. Geosci.*, 344, 516-525, <https://doi.org/10.1016/j.crte.2012.09.004>.
- Rozenbaum O., and Rolland du Roscoat S., 2014.** Representative elementary volume assessment of three-dimensional X-ray microtomography images of heterogeneous materials: Application to limestones. *Phys. Rev. E*, 89: 053304. <https://doi.org/10.1103/PhysRevE.89.053304>.
- Smith S.W., 1997.** The scientist and engineer's guide to digital signal processing. California Technical Publishing, San Diego, CA, USA.
- Swinnen W., Broothaerts N., and Verstraeten G., 2021.** Modelling long-term alluvial peatland dynamic in temperate river flood plains, *Biogeosciences Discuss* (preprint), <https://doi.org/10.5194/bg-2021-132>, in review.
- Turberg P., Zeimetz F., Grondin Y., Elandoy C., and Buttler A., 2014.** Characterization of structural disturbances in peats by X-ray CT-based density determinations. *Eur. J. Soil Sci.*, 65, 613-624. <https://www.dora.lib4ri.ch/wsl/islandora/object/wsl:5128>.
- Vogel H.J., 2002.** Topological characterization of porous media. 2nd Int. Wuppertal Workshop Statistical Physics and Spatial Statistics, University of Wuppertal, March 5-9, 2001 Wuppertal, Germany, In: *Physics and geometry of spatially complex systems*, Lecture Notes in Physics (Eds K. Mecke and D. Stoyan) Morphology of condensed matter: Springer, 600, 75-92.
- Wang S., Yang Z., and Yang P., 2017.** Structural change and volumetric shrinkage of clay due to freeze-thaw by 3D X-ray computed tomography. *Cold Reg. Sci. Technol.*, 138, 108-116. <https://doi.org/10.1016/j.coldregions.2017.03.007>.
- Wiedeveld S.Th.J., van den Berg M., and Lamers L.P.M., 2021.** Conventional subsoil irrigation techniques do not lower carbon emissions from drained peat meadows. *Biogeosciences*, 18, 3881-3902, <https://doi.org/10.5194/bg-18-3881-2021>.
- Youn H., Kim H.K., Kam S., Kim S.H., Park J.W., and Jeon H., 2015.** Physics-based modeling of computed tomography systems. Conf. Medical Imaging – Physics of Medical Imaging, February 22-25, Orlando, FL, In: *Medical imaging 2015: Physics of medical imaging* (Eds C. Hoeschen and D. Kontos). Proc. SPIE, 9412: 94122N.
- Zhao H.F., Muraro S., and Jommi C., 2020.** Gas exsolution and gas invasion in peat: towards a comprehensive modelling framework. *Géotechnique Letters*, 10(3), 461-467, <https://doi.org/10.1690/jgele.20.00014>.